

Turbulent boundary layer structure identification via POD

By J. R. Baltzer[†], R. J. Adrian[†] AND X. Wu[‡]

Proper orthogonal decomposition (POD) is applied to the direct numerical simulation (DNS) of a turbulent boundary layer performed by Wu & Moin (2010), and the resulting POD modes of various scales are examined. The modes include structures resembling those observed in instantaneous flow fields, such as large-scale motions of streamwise velocity with ramp-like wall-normal growth. Other modes correspond closely to near-wall streaks. In addition, POD modes that are constant across the spanwise domain width are observed to grow from the wall with the mean boundary layer thickness. The results support the existence of boundary layer coherent motions described by the hairpin packet model (Adrian 2007).

1. Introduction

Coherent motions in wall-bounded turbulent flows have been the subject of recent study, but questions remain about the organization and form of coherent structures (Adrian 2007). One method of extracting coherent structures is POD (Lumley 1981; Holmes *et al.* 1998). POD extracts modes that are linearly combined to form each flow field snapshot, with the reconstruction by partial sums of POD modes converging faster than by any other set of orthogonal functions in a mean energy sense (Liu *et al.* 2001).

POD has been successfully applied to wall-bounded turbulent flows including three-dimensional DNS data sets. Moin & Moser (1989) calculated POD modes for a $Re_\tau = 180$ turbulent channel DNS simulation and focused on obtaining compact structures. Since the resulting POD modes span a wide range of spatial scales as large as the domain, they were interpreted using a method proposed by Lumley (1981) in which characteristic eddies were assembled from POD modes with phases chosen to make the eddies compact. The method assumed characteristic eddies to be scattered randomly in the homogeneous streamwise and spanwise coordinates.

Recent attention has focused on large-scale motions (LSMs) and very large-scale motions (VLSMs), also known as superstructures, observed in wall-bounded shear flows (e.g. Kim & Adrian 1999; Hutchins & Marusic 2007). Examining these motions requires interpretations of POD modes that preserve the large scales instead of assembling compact motions. Liu *et al.* (2001) employed POD to analyze two-dimensional velocity measurements of a turbulent channel including studying the LSMs and VLSMs. They examined individual POD modes and considered projections of fields onto sets of modes (partial reconstructions). Although POD in a homogeneous direction is simply a Fourier mode, this is appropriate for analyzing these motions because LSMs and VLSMs are often defined in terms of Fourier spectra. The results indicated that a set of several large-scale POD modes were associated with large contributions to the turbulent kinetic energy and Reynolds stress. The patterns of motion revealed by projections onto sets of POD modes

[†] School for Engineering of Matter, Transport and Energy, Arizona State University

[‡] Department of Mechanical Engineering, Royal Military College of Canada

were consistent with the hairpin packet paradigm (Adrian *et al.* 2000), in which hairpin-shaped vortical structures are understood to arrange in streamwise x -aligned packets, and thereby contribute to long structures. Adrian *et al.* (2000) frequently observed ramps of retarded streamwise velocity with wall-normal growth angles of approximately 10-20° relative to $+x$ as evidence of hairpin packets in turbulent boundary layers.

While POD has also been applied to DNS of turbulent pipes (e.g. Duggeby & Paul 2010), there have been no recent three-dimensional applications to turbulent boundary layer flows, although structures in transition were studied with POD by Rempfer & Fasel (1994). Recent incompressible zero-pressure-gradient flat-plate turbulent boundary layer simulations of Wu & Moin (2009) periodically introduced blocks of isotropic turbulence into the laminar flow at the inlet and allowed the boundary layer to progress through transition. Hairpin-shaped vortical structures were more clearly visible in this simulation compared to previous simulations with artificially generated turbulent inflows. Wu & Moin (2010) extended the simulation to a longer streamwise domain so the flow would evolve from $Re_\theta = 80$ to 1950 and increased the spanwise domain width. With the clear structures observed in this simulation, POD is an appropriate tool to extract structural information from this data set.

We apply POD to the entire DNS fields of this simulation including the transition region. The choice of domain is relevant because the POD equation and orthogonality between POD modes are defined by an inner product over a specified domain (§2). The POD modes decompose the fluctuating velocity field. The inner product involves all three velocity components, so the resulting POD modes also include contributions of all velocity components.

2. Method

POD is performed on the flow using the conventional norm such that optimality of convergence exists in the energy sense. The standard POD equation for the three-dimensional vector field of velocity fluctuation \mathbf{u} based on an expansion of the form $\mathbf{u}(\mathbf{x}) = \sum_{n=1}^N a_n \Phi(\mathbf{x})$ is

$$\int_{\mathcal{D}} \mathbf{R}(\mathbf{x}, \mathbf{x}') \Phi(\mathbf{x}') d\mathbf{x}' = \lambda \Phi(\mathbf{x}), \quad (2.1)$$

with the two-point spatial correlation $\mathbf{R}(\mathbf{x}, \mathbf{x}') = \langle \mathbf{u}(\mathbf{x}) \otimes \mathbf{u}^*(\mathbf{x}') \rangle$ (Holmes *et al.* 1998).

The boundary layer is homogeneous and periodic in z , so POD modes converge to trigonometric functions in z , and it is appropriate to enforce this behavior by expressing the velocity components u_i as Fourier series expansions,

$$u_i(x, y, z, t) = \sum_{k_z=-N_z/2+1}^{N_z/2} \hat{u}_i^{(k_z)}(x, y, t) e^{2\pi\sqrt{-1} \frac{k_z z}{L_z}}. \quad (2.2)$$

This procedure has been employed in several applications (e.g., Freund & Colonius 2009; Duggeby & Paul 2010), and has been shown to improve the statistical convergence of POD because it incorporates information from all possible shifts of the homogeneous coordinate. Then, a POD expansion is used to represent the Fourier coefficients $\hat{u}_i^{(k_z)}(x, y, t)$:

$$\hat{u}_i^{(k_z)}(x, y, t) = \sum_{n=1}^N \hat{a}^{(k_z, n)}(t) \hat{\phi}_i^{(k_z, n)}(x, y). \quad (2.3)$$

The inhomogeneity of both x and y results in a direct POD (2.1) problem with a

very large correlation matrix of averages calculated over the series of flow field snapshots spaced in time. The number of snapshots is significantly fewer than the number of points involved, so calculating the POD modes using the *method of snapshots* (Sirovich 1987) greatly reduces the computation necessary. While mathematically equivalent, the eigenproblem is performed on time correlations instead of spatial correlations. This method is derived (Sirovich 1987) by expressing the POD modes as linear combinations of the N_t snapshots $\hat{\phi}_i^{(k_z, n)}(x, y) = \sum_{j=1}^{N_t} c_j^{(k_z, n, t_j)} \hat{u}_i^{(k_z)}(x, y, t_j)$. Then, the eigenproblem (2.1) becomes an eigenproblem to solve for the coefficients c

$$\sum_{j=1}^{N_t} \mathbf{M}_{hj}^{(k_z)} c_j^{(k_z)} = \lambda^{(k_z)} c_h^{(k_z)}, \quad (2.4)$$

where the $\mathbf{M}_{hj}^{(k_z)}$ matrix contains the time correlations. For the present problem, these time correlations are between Fourier coefficients

$$\mathbf{M}_{hj}^{(k_z)} = \int_0^{L_y} \int_0^{L_x} \hat{u}_i^{(k_z)}(x, y, t_j) \hat{u}_i^{*(k_z)}(x, y, t_h) dx dy = \left(\hat{\mathbf{u}}^{(k_z)}(x, y, t_j), \hat{\mathbf{u}}^{(k_z)}(x, y, t_h) \right) \quad (2.5)$$

(summation assumed on repeated indices) (Freund & Colonius 2009). Integration is approximated by the trapezoidal rule, which is satisfactory for POD (Moin & Moser 1989).

The POD modes obtained from the snapshot method are normalized to satisfy orthonormality as $\int_0^{L_y} \int_0^{L_x} \hat{\phi}_i^{(k_z, n)}(x, y) \hat{\phi}_i^{*(k_z, n)}(x, y) dx dy = \delta_{mn}$. The POD coefficients to reconstruct each velocity field in (2.3) are obtained from

$$\hat{a}^{(k_z, n)}(t) = \int_0^{L_y} \int_0^{L_x} \hat{u}_i^{(k_z)}(x, y, t) \hat{\phi}_i^{*(k_z, n)}(x, y) dx dy. \quad (2.6)$$

Due to the conjugate symmetry $\hat{\phi}_i^{(k_z, n)}(x, y) = \hat{\phi}_i^{*(-k_z, n)}(x, y)$, computing only the non-negative k_z modes is sufficient to reconstruct the real-valued velocity. Mode indices n are numbered by decreasing eigenvalue, with $n = 1$ contributing most energy.

As discussed in Wu & Moin (2010), a Blasius profile with momentum thickness θ_0 is specified at the inlet. The computational domain dimensions are $12750\theta_0$, $2250\theta_0$, and $562.5\theta_0$ in the streamwise x , wall-normal y , and spanwise z coordinates, respectively. The corresponding numbers of grid points are $N_x = 8192$, $N_y = 500$, and $N_z = 256$. The POD modes were calculated from a collection of $N_t = 54$ DNS flow field snapshots separated in time by at least $150\theta_0/U_\infty$. The mean velocities were obtained using frequent sampling during the original simulation run and are better converged than if they were obtained from the 54 fields available. Both time averaging and spatial averaging in the homogeneous z coordinate are used to calculate the mean velocities for obtaining the fluctuation velocities.

3. Results

The fluctuating velocity of a DNS field is reconstructed by (2.2) and (2.3):

$$u_i(x, y, z) = \sum_{k_z=-N_z/2+1}^{N_z/2} \sum_{n=1}^N \hat{a}^{(k_z, n)} \hat{\phi}_i^{(k_z, n)}(x, y) e^{2\pi\sqrt{-1}\frac{k_z z}{L_z}} = \sum_{k_z=-N_z/2+1}^{N_z/2} \sum_{n=1}^N u_i^{(k_z, n)}(x, y, z). \quad (3.1)$$

k_z	$n = 1$	$n = 2$	$n = 3$	$n = 4$	$n = 5$	$n = 6$	$n = 1-16$	$n = 1-54$
0	2.95%	2.72%	0.38%	0.36%	0.34%	0.30%	9.04%	11.36%
± 1	1.11%	0.77%	0.64%	0.58%	0.53%	0.50%	7.49%	12.64%
± 2	0.67%	0.60%	0.52%	0.49%	0.47%	0.41%	6.27%	11.71%
± 3	0.73%	0.40%	0.37%	0.35%	0.33%	0.32%	4.99%	9.81%
± 4	0.35%	0.32%	0.28%	0.27%	0.25%	0.24%	3.66%	7.85%
± 5	0.23%	0.23%	0.22%	0.21%	0.20%	0.19%	2.85%	6.36%

TABLE 1. Eigenvalues (λ/E).

Each mode's contribution is $u_i^{(k_z, n)} = \hat{a}^{(k_z, n)} \hat{\phi}_i^{(k_z, n)} e^{2\pi\sqrt{-1} \frac{k_z z}{L_z}} = \hat{a}^{(k_z, n)} \phi_i^{(k_z, n)}$. Liu *et al.* (2001) discussed visualization and interpretation of individual POD modes, and similar principles apply to the present results. The POD coefficient \hat{a} specifies the magnitude and phase (which corresponds to a spanwise shift of the entire field in physical space) of each modal contribution, so visualizing only the real part reveals all of the features for each mode. Liu *et al.* (2001) show that the imaginary part of $\phi_i^{(k_z, n)}$ is equal to the real part of $\phi_i^{(k_z, n)}$ after applying a $\pi/2$ phase shift, which is a spatial shift of $L_z/(4k_z)$. The mode contributions $u_i^{(k_z, n)}$ are linear combinations of the real parts of $\phi_i^{(k_z, n)}$ with and without the shift, so examining only the real part is sufficient. The real part of $\phi_i^{(k_z, n)}$ is equal to the $u_i^{(k_z, n)}$ contribution of a $\pm k_z$ mode pair with $\hat{a}^{(k_z, n)} = 0.5$.

Figure 1 contains isosurfaces of streamwise velocity for this real part of a representative selection of individual POD modes. The sign of velocity is arbitrary because the sign is dictated by $\hat{a}^{(k_z, n)}$, and a phase shift of π reverses the sign of velocity at a given location. With this sinusoidal dependence, velocity structures of opposite sign and the same shape are present in spanwise locations between the structures shown in the isosurfaces. The oblique perspective from above the flat plate highlights the organization of the u velocity structures that take the form of long streamwise streaks. Figure 2 contains similar plots for $k_z = 20$.

Contour plots of u in x - y planes for two $k_z = 0$ modes are presented in Figure 3. The boundary layer thickness $\delta(x)$, defined as the y where mean velocity is 99% of free-stream, is included as a line. The $n = 1$ mode (a,b), which is responsible for the largest mean energy contribution to the flow, consists of alternating regions of positive and negative u velocity fluctuations with wall-normal growth closely matching the boundary layer thickness. The $n = 2$ mode (not shown) is similar except that the streamwise positions of the structures are shifted by one quarter period, and $n = 1$ and $n = 2$ mode eigenvalues are comparable. This is similar to the sinusoidal modes that would occur if the flow were homogeneous in x (as in the case of a channel) but with wall-normal growth for the boundary layer and decay in strength. These features are also consistent with modes for traveling waves, as discussed by Aubry *et al.* (1992). Although blocks of isotropic turbulence were periodically introduced at intervals of $3131.45\theta_0/U_\infty$ for this simulation (Wu & Moin 2010), the streamwise period of the structures in the mode is significantly shorter. The $n = 4$ mode (c,d) includes similar structures of alternating u fluctuation in the transitional region but with shorter wavelength. These structures are less distinct in the second half of the domain (d). This mode also includes contributions associated with the isotropic turbulence blocks that are apparent above the boundary layer thickness.

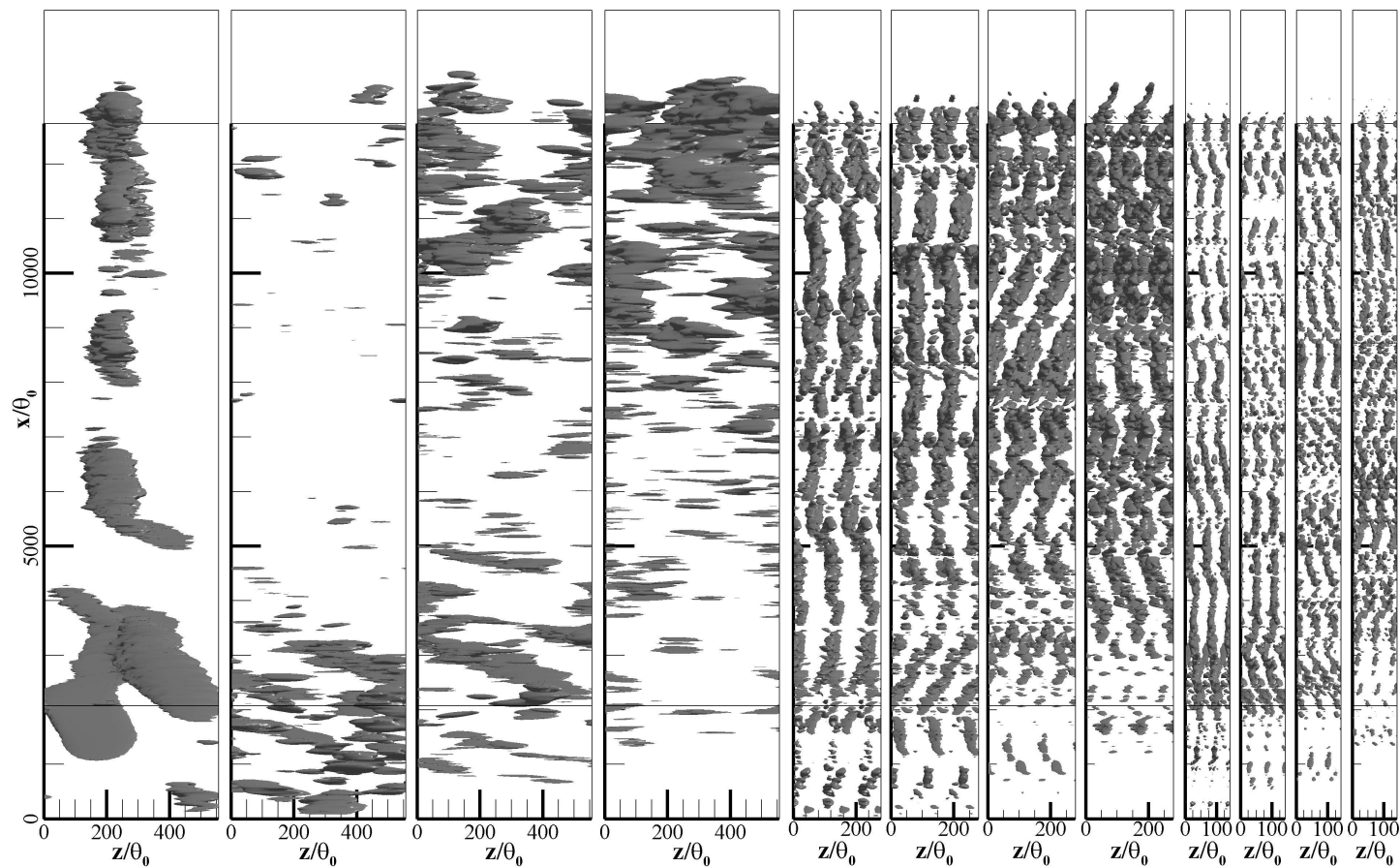


FIGURE 1. Streamwise velocity isosurfaces of POD modes arranged in sets of constant k_z , with $k_z = 1, 5, 10$ shown from left to right. Within each group, mode numbers $n = 1, 5, 10, 20$ are shown. Approximately two spanwise periods are shown for compactness, except for the $k_z = 1$ modes where the entire domain is shown. Visualizations of the other fields have the same scale. The modes are viewed obliquely from above the flat plate.

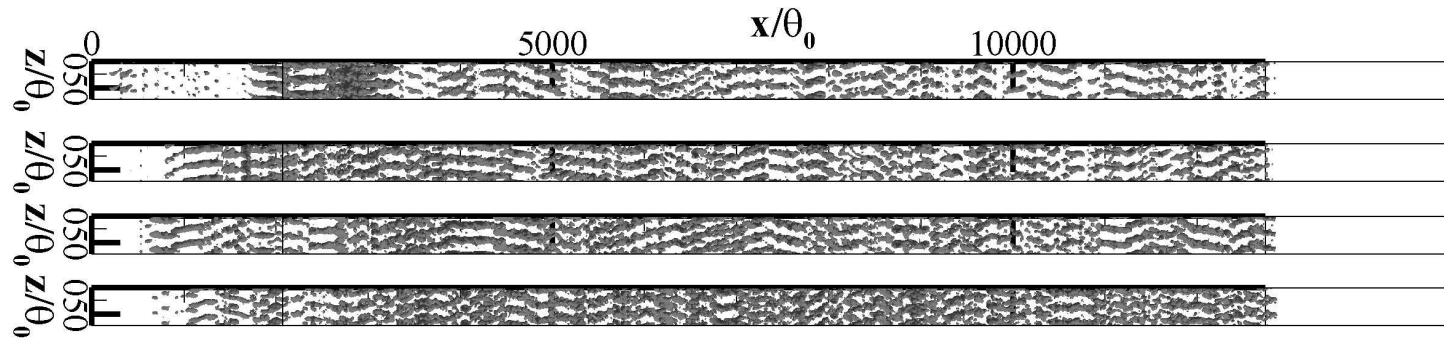


FIGURE 2. Streamwise velocity isosurfaces of POD modes for $k_z = 20$ and $n = 1, 5, 10, 20$ (top to bottom).

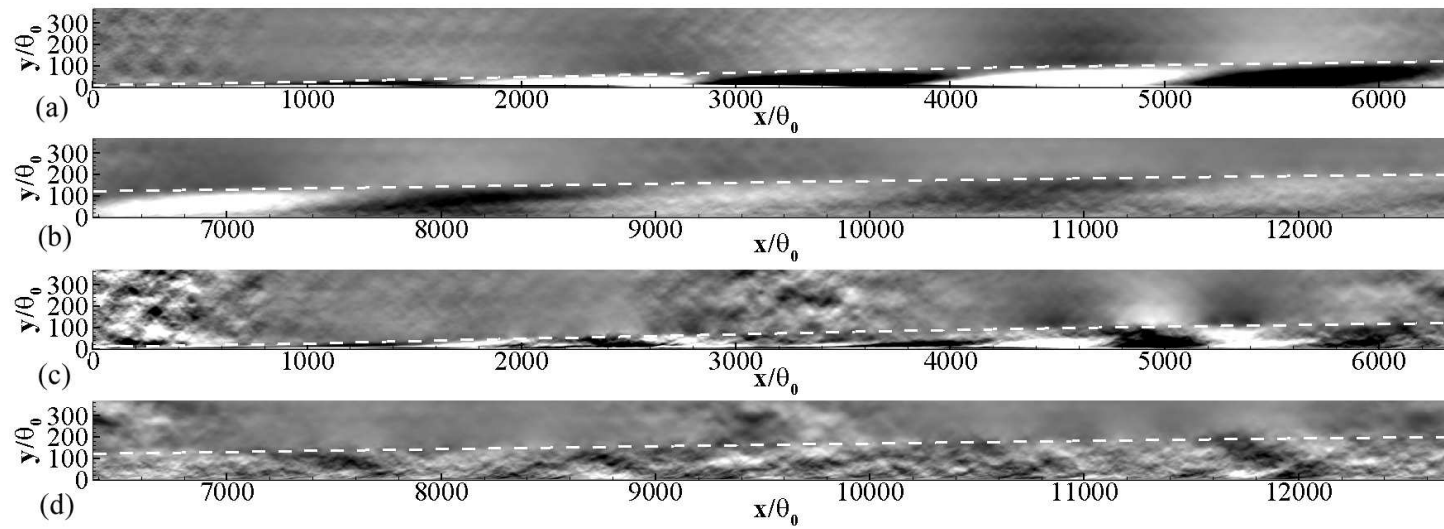


FIGURE 3. Planes of the $n = 1$ (a,b) and $n = 4$ (c,d) $k_z = 0$ modes shaded by streamwise velocity for each streamwise half of the domain. The dotted white line indicates the boundary layer thickness $\delta(x)$.

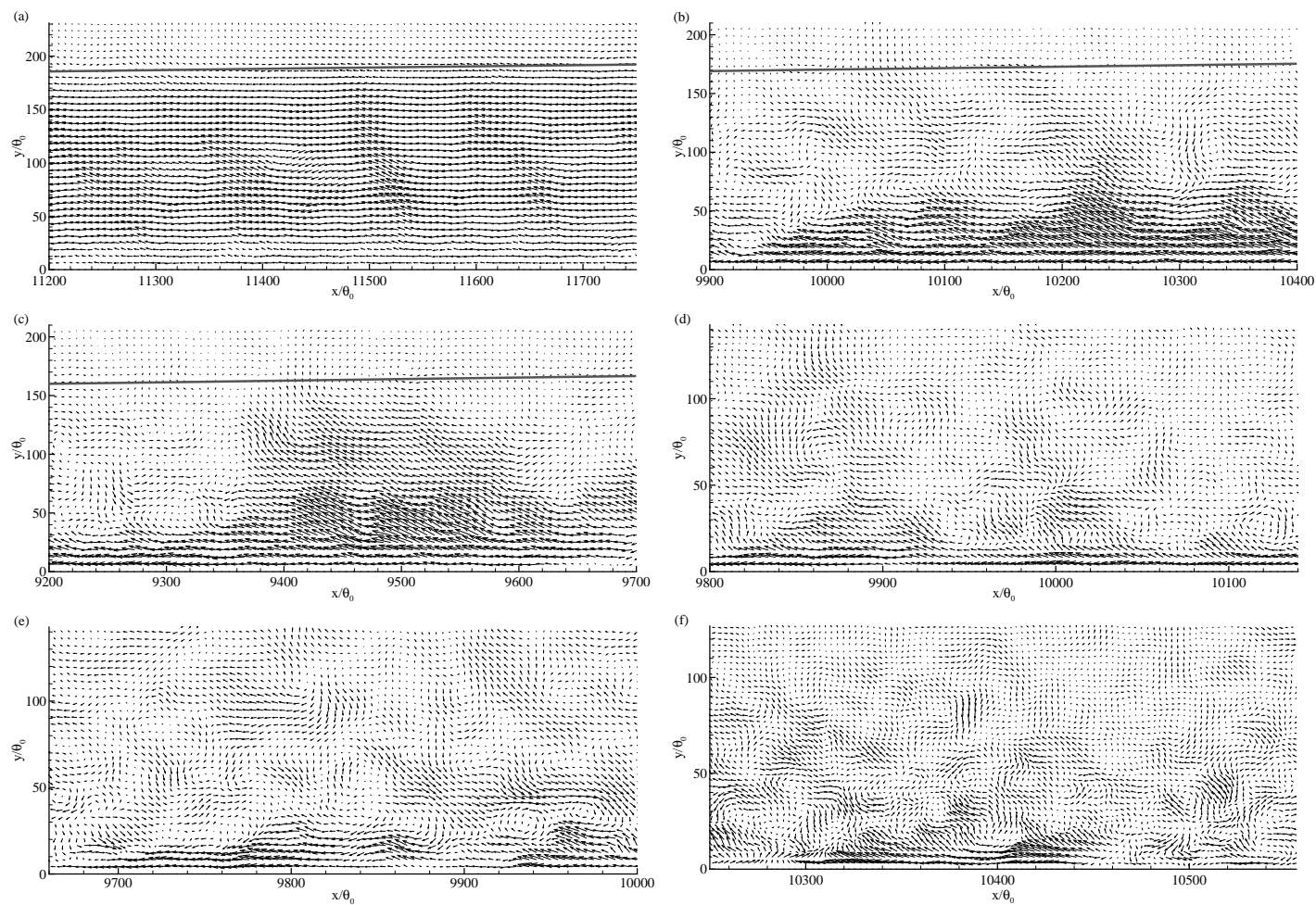


FIGURE 4. (a) $k_z = 1, n = 1$, (b) $k_z = 5, n = 1$, (c) $k_z = 5, n = 5$, (d) $k_z = 10, n = 1$, (e) $k_z = 10, n = 5$, and (f) $k_z = 20, n = 1$ mode velocity.

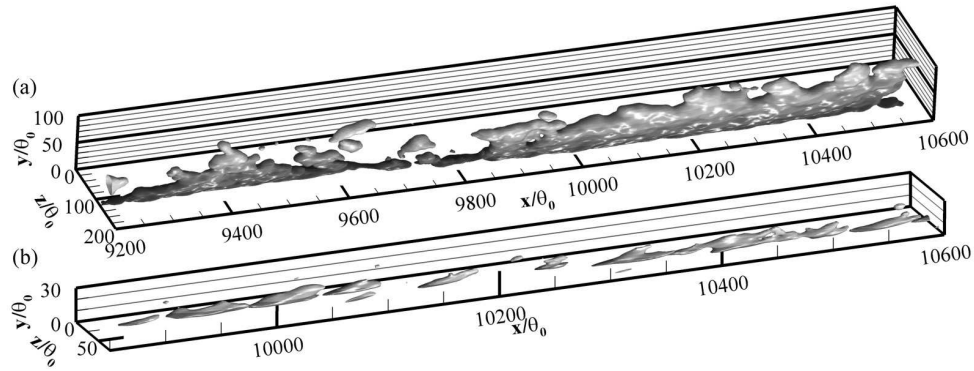


FIGURE 5. u isosurfaces for (a) $k_z = 5, n = 1$ and (b) $k_z = 20, n = 1$ POD modes.

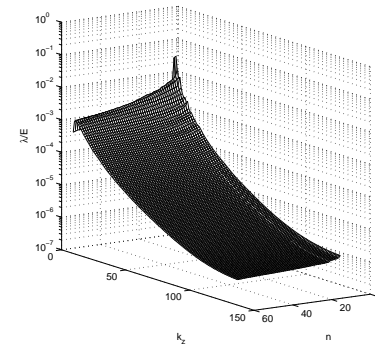


FIGURE 6. POD mode eigenvalues.

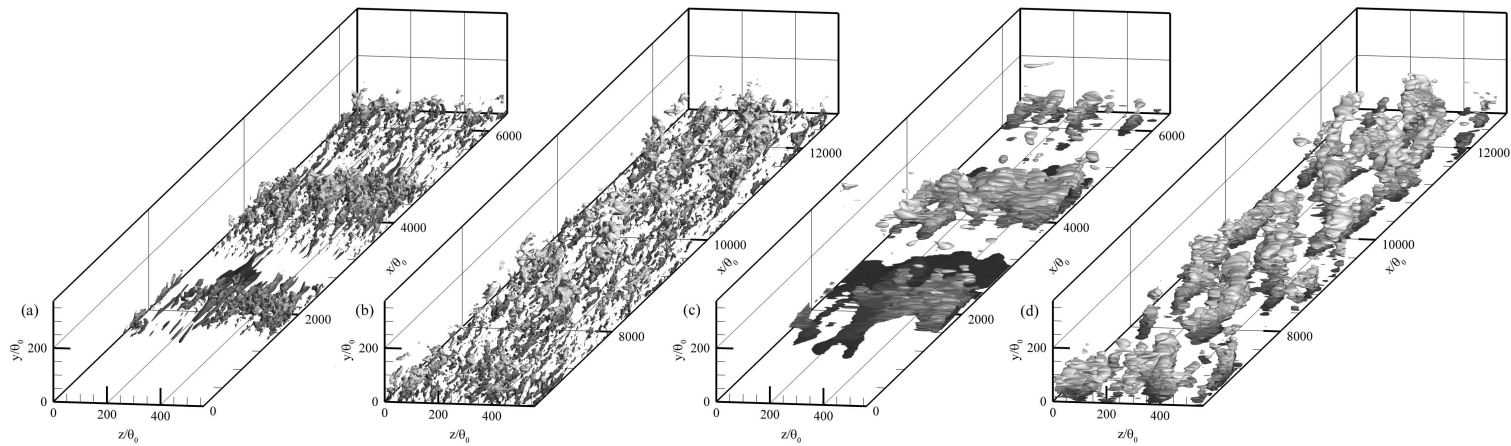


FIGURE 7. Negative u isosurfaces (shaded by y) of one DNS field (a,b) and its reconstruction with $k_z = 0 - 5$ and $n = 1 - 16$ POD modes (c,d).

Figure 4 presents vector plots of planes extracted at spanwise locations where the negative u structures are strongest. Boundary layer thickness $\delta(x)$ is also included as a gray line. As spanwise wavenumber index k_z increases, the wall-normal height of u structures decreases for the most energetic mode numbers ($n = 1$ and 5 shown). The shorter ramps are clearly apparent in the u isosurfaces of Figure 5. The $k_z = 5$ structures are consistent with the ramp structures associated with hairpin packets, which are discussed by Adrian *et al.* (2000). The vector plots (Figure 4b,c) indicate the negative velocity structures are associated with positive wall-normal velocity. Steeply inclined regions of these quadrant 2 ejections below a swirling hairpin head pattern are identified as the signature of hairpin vortices which organize to form hairpin packets (Adrian *et al.* 2000). These modes contain evidence of such structures with streamwise lengths of several δ (consistent with large-scale motions), but other modes that include finer scales also contribute to details of the vortices. Although POD is used instead of linear stochastic estimation, this analysis is similar to that of Christensen & Adrian (2001), in that statistically important structures are extracted and shown to be consistent with hairpin packet structures. The present calculation is successful in extracting relevant structures, although statistical convergence of the POD modes would improve with additional snapshots.

For the mode with $k_z = 20$ and $n = 1$, the strongest structures are centered about $y/\theta_0 \approx 5$, which corresponds to $y^+ = 15$ in this region, although they can extend up to $y^+ = 75$. The spanwise wavelength associated with the $k_z = 20$ modes is approximately 100^+ , which is the accepted near-wall streak spacing λ^+ . These features suggest that this mode corresponds to the near-wall velocity streak motions.

The spectrum shown in Figure 6 contains the eigenvalues, with values representing the mean energy of pairs with wavenumber indices $\pm k_z$ because modes must contribute in pairs for the velocity to be real valued. The n index is responsible for the various scales in both the inhomogeneous streamwise and wall-normal directions, whereas k_z represents scale in only the spanwise coordinate. Therefore, the eigenvalue decay is slower in n than in k_z . E represents the mean turbulent kinetic energy, and the sum of all λ/E displayed is unity. The spectrum indicates much of the energy is contained in low k_z modes, and Table 1 summarizes the contributions with $n = 1-54$ including all POD modes.

From the projection of one DNS field onto the POD modes, a partial reconstruction is generated using a set of the most energetic modes with $k_z = 0-5$ and $n = 1-16$. Omitting spanwise Fourier modes effectively applies a low-pass cutoff filter. Figure 7 compares negative u fluctuation isosurfaces for the original DNS field and POD partial reconstruction. Since the omitted modes of smaller scales contribute to the velocity peaks, a lower threshold is chosen to plot the isosurfaces of the reconstructed field. The reconstruction indicates how large-scale motions evolve from transition to the fully turbulent regions. It is apparent from the reconstruction that the $k_z = 0$ modes with no spanwise variation (discussed in connection with Figure 3) make significant contributions to the flow, which is consistent with their large eigenvalues.

4. Conclusions

POD modes for a turbulent boundary layer reveal structures that can be identified with features observed instantaneously in the flow. The velocity structures include near-wall streaks and ramps consistent with the hairpin vortex paradigm. The POD modes revealing these structures are useful because they represent patterns of these structures that are statistically significant and likely appear frequently. The negative u ramp segments

for the $k_z = 5$ modes shown in Figure 1 may indicate characteristic lengths of hairpin packets and the spatial patterns suggest how packets organize. The spanwise drifts and staggering are physically significant and show that POD modes contain useful spanwise information despite the trigonometric behavior. POD also identified modes consistent with traveling waves that decay and grow in scale, and further analysis can address how their form may be affected by the isotropic turbulence introduced at the inlet and how this influences the structure downstream. Tracking the time evolution of the POD mode coefficients and partial reconstructions would reveal further flow physics.

The authors wish to acknowledge the generous support of the Center for Turbulence Research. This research was also supported by NSF Award CBET-0933848.

REFERENCES

- ADRIAN, R. J. 2007 Hairpin vortex organization in wall turbulence. *Phys. Fluids* **19**, 041301.
- ADRIAN, R. J., MEINHART, C. D. & TOMKINS, C. D. 2000 Vortex organization in the outer region of the turbulent boundary layer. *J. Fluid Mech.* **422**, 1–54.
- AUBRY, N., GUYONNET, R. & LIMA, R. 1992 Spatio-temporal symmetries and bifurcations via biorthogonal decompositions. *J. Nonlinear Sci.* **2**, 183–215.
- CHRISTENSEN, K. T. & ADRIAN, R. J. 2001 Statistical evidence of hairpin vortex packets in wall turbulence. *J. Fluid Mech.* **431**, 433–443.
- DUGGLEBY, A. & PAUL, M. R. 2010 Computing the Karhunen-Loève dimension of an extensively chaotic flow field given a finite amount of data. *Computers & Fluids* **39**, 1704–1710.
- FREUND, J. B. & COLONIUS, T. 2009 Turbulence and sound-field POD analysis of a turbulent jet. *International Journal of Aeroacoustics* **8**, 337–354.
- HOLMES, P., LUMLEY, J. L. & BERKOOZ, G. 1998 *Turbulence, Coherent Structures, Dynamical Systems and Symmetry*. Cambridge University Press.
- HUTCHINS, N. & MARUSIC, I. 2007 Evidence of very long meandering features in the logarithmic region of turbulent boundary layers. *J. Fluid Mech.* **579**, 1–28.
- KIM, K. C. & ADRIAN, R. J. 1999 Very large-scale motion in the outer layer. *Phys. Fluids* **11**, 417–422.
- LIU, Z.-C., ADRIAN, R. J. & HANRATTY, T. J. 2001 Large-scale modes of turbulent channel flow: transport and structure. *J. Fluid Mech.* **448**, 53–80.
- LUMLEY, J. L. 1981 Coherent structures in turbulence. In *Transition and Turbulence* (ed. R. E. Meyer), pp. 215–241. Academic.
- MOIN, P. & MOSER, R. D. 1989 Characteristic-eddy decomposition of turbulence in a channel. *J. Fluid Mech.* **200**, 471–509.
- REMPFER, D. & FASEL, H. F. 1994 Evolution of three-dimensional coherent structures in a flat-plate boundary layer. *J. Fluid Mech.* **260**, 351–375.
- SIROVICH, L. 1987 Turbulence and the dynamics of coherent structures, Parts I, II and III. *Quarterly of Applied Mathematics* **XLV**, 561–590.
- WU, X. & MOIN, P. 2009 Direct numerical simulation of turbulence in a nominally zero-pressure-gradient flat-plate boundary layer. *J. Fluid Mech.* **630**, 5–41.
- WU, X. & MOIN, P. 2010 Transitional and turbulent boundary layer with heat transfer. *Phys. Fluids* **22**, 085105.